Science & Technology Development Journal 2024, ():1-10

Open Access Full Text Article

Research article

Visible light-driven activation of peroxymonosulfate for boosting tetracycline degradation using B-doped g-C_3N_4 nanotubes

Nguyen Thuy Giang[1,2], Nguyen Duy Hai[1], Phan Dinh Quang[3], Vu Hoang Huong[4], Nguyen Viet Hung[5], Nguyen Manh Dung[6,*]

ABSTRACT

Using photocatalysis to activate peroxymonosulfate (PMS) under visible light is an intriguing possibility for removing contaminants from wastewater. Since its discovery as a powerful photocatalyst, g-C_3N_4 has attracted the interest of researchers due to its ability to activate PMS for removal of organic contaminants. In this study, we report the preparation of boron-doped g-C_3N_4 nanotubes (1DBCN) produced through a simple calcination technique that effectively photodegraded tetracycline (TC) with PMS activators under visible light. 1DBCN exhibits 99% of TC using a catalyst of 0.5 g/L and 0.3 mM PMS at pH 7 within 30 minutes. Moreover, the study extensively analyzed the effect of PMS concentration and proposed a potential reaction mechanism. The introduction of B in graphitic carbon nitride (GCN) nanotubes reduces the band gap and broadens the visible light absorption range. The combined unique nanotube morphology and doping contributed to the exceptional photocatalytic performance exhibited by the synthesized photocatalyst nanotubes. Overall, this research contributes to the development of advanced oxidation processes and sustainable water treatment technologies by utilizing visible-light-driven photocatalysis for the removal of organic pollutants from wastewater.

Key words: Graphitic carbon nitride nanotubes, photocatalytic degradation, tetracycline (TC), peroxymonosulfate, visible light

INTRODUCTION

In recent years, there has been an increase in the number of patients worldwide during the COVID-19 crisis, resulting in a significant increase in the daily consumption of antibiotics. Tetracycline (TC), an antibiotic, is extensively utilized for the treatment of human diseases, veterinary applications and agricultural development [1]. Unfortunately, TC has been detected in various water sources, including groundwater, surface water, and even drinking water, posing a severe threat to human health and the environment [2]. Various treatment technologies, such as adsorption, biodegradation, and membrane filtration, have been developed to address this issue. However, the implementation of these technologies is often hindered by their high cost and high energy requirements, making it challenging to adopt them in certain regions [3]. Consequently, there is a pressing need to develop more efficient and cost-effective TC removal technologies.

Since then, advanced oxidation processes (AOPs) based on PMS have been increasingly developed. These AOPs have shown promise in addressing the challenges of removing organic pollutants and have expanded their applications beyond water treatment. They have demonstrated effectiveness in air purification and the remediation of contaminated soil and sediments, highlighting the versatility of PMS-based AOPs in different remediation scenarios. The activation of PMS generates reactive sulfate radicals ($SO_4^{\bullet-}$) as well as other nonradical species, including singlet oxygen ($^1O_2$).

These species play a crucial role in decomposing organic pollutants through oxidation reactions [4]. To activate PMS, various methods can be employed, including the use of carbon materials, transition metals, ultrasound, heat, and electricity. However, photocatalysis, which utilizes visible light to activate the PMS reaction, is a promising approach for energy efficiency and cost reduction. In particular, visible-light-driven photocatalysis using graphitic carbon nitride (g-C_3N_4, GCN) is a favorable option for PMS activation due to its high stability, low cost, and facile synthesis [5]. As a type of photocatalyst, GCN can absorb visible light and transfer energy to electrons, leading to the generation of reactive oxygen species (ROS) and holes capable of decomposing organic molecules. Additionally, the photoexcited electrons generated in GCN can contribute to the activation of PMS, consequently leading to increased ROS production [6].

[1]*Thai Nguyen University of Agriculture and Forestry, Thai Nguyen City, Viet Nam*

[2]*Thai Nguyen University of Medicine and Pharmacy, Thai Nguyen City, Viet Nam*

[3]*Vietnam National Institute of Occupational Safety and Health, 99 Tran Quoc Toan, Hoan Kiem, Hanoi 100000, Viet Nam*

[4]*University of Science, Vietnam National University, Hanoi 100000, Viet Nam*

[5]*Vietnam Academy for Ethnic Minorities, Hanoi 100000, Viet Nam*

[6]*Research Institute for Natural Resources and Climate Change, Hanoi University of Natural Resources and Environment, Hanoi 100000, Viet Nam*

Correspondence

Nguyen Manh Dung, Research Institute for Natural Resources and Climate Change, Hanoi University of Natural Resources and Environment, Hanoi 100000, Viet Nam

Email: nmdung@hunre.edu.vn

Cite this article : Giang N T, Hai N D, Quang P D, Huong V H, Hung N V, Dung N M. **Visible light-driven activation of peroxymonosulfate for boosting tetracycline degradation using B-doped g-C_3N_4 nanotubes**. *Sci. Tech. Dev. J.* 2024; ():1-10.

History
• Received:
• Accepted:
• Published Online:

DOI :

However, pristine GCN still suffers from a high electron-hole recombination rate, leading to a low PMS activation capacity. Nanostructures such as one-dimensional (1D) porous nanotubes are attractive nanostructures for GCN due to their high surface area and multiple active sites. The elongated structure of the nanotubes creates a resonant cavity that can trap light, allowing for multiple reflections and improved photocatalytic performance. Moreover, boron (B) doping of GCN can delocalize electrons from sp^2-hybridized carbon, thus enhancing the activation of PMS for radical production[7]. Recent studies have successfully fabricated highly recyclable boron-doped graphitic carbon nitride (BCN) photocatalyst films. These materials exhibited superior photocatalytic cyclic stability, attributed to their extended visible-NIR light absorption. Notably, the optimized composition achieved up to 95% rhodamine B degradation after 2 hours of irradiation[8]. Additionally, boron-doped GCN photocatalysts have been synthesized from melamine and boron oxide. Interestingly, these materials demonstrated different dye degradation mechanisms depending on the dye. While rhodamine B degradation proceeded via direct hole oxidation, methyl orange degradation was primarily driven by the reduction process initiated by photogenerated electrons[9].

In this study, we aimed to address the above challenges and contribute to the development of efficient TC removal technologies. We have developed a facile and environmentally friendly one-step method for the synthesis of boron-doped GCN nanotubes using melamine and urea precursors. Compared to other fabrication methods, this approach offers a high surface area, which is crucial for efficient photocatalytic performance. The unique aspect of this research lies in the combination of B-doped GCN nanotubes with PMS for the photocatalytic degradation of TC. To the best of our knowledge, no previous studies have been published on the use of B-doped GCN nanotubes in conjunction with PMS for TC photocatalytic degradation.

In summary, this study aimed to develop a simple method to synthesize boron-doped GCN nanotubes using melamine, urea and boric acid as precursors for the photocatalytic degradation of tetracycline. Investigations were conducted to assess the impact of various factors, including the concentration of the photocatalyst and peroxymonosulfate (PMS), as well as to identify the primary reactive oxygen species (ROS) generated during the reaction process. These findings will contribute to future research and exploration in designing and developing cost-effective materials for efficient TC removal.

MATERIALS AND METHODS

Chemicals and reagents

Peroxymonosulfate ($KHSO_5 \cdot 0.5KHSO_4 \cdot 0.5K_2SO_4$), melamine, urea, and boric acid were obtained from Merck, Sigma and used without further purification. All the solutions were prepared in ultrapure water from a purification system.

Preparation of B-doped GCN nanotubes (1DBCN)

A mixture of melamine (1 g), urea (10 g), and boric acid (0.1 g) in a mass ratio was calcined at 600°C for 4 hours at a rate of 10°C/min in air to produce 1DBCN nanotubes[10]. The undoped GCN nanotubes used the same procedure without boric acid (labeled 1DGCN). Following the same method, a 2D nanosheet was prepared using a mass ratio of melamine (1 g) to urea (1 g), denoted as 2DGCN.

Characterizations of photocatalysts

The morphology of the synthesized samples was analyzed utilizing a field-emission scanning electron microscope (Hitachi S-4800) operating at 15 kV. The presence of elements was identified through the application of SEM energy dispersive X-ray spectroscopy (EDS). An X-ray diffractometer (XRD, Bruker D8 Advance, Billerica, MA, USA) was used to investigate the crystal structures of the photocatalyst materials utilizing Ni-filtered Cu Kα radiation (λ = 1.5406 Å). The XRD measurements were performed at 40 kV and 40 mA, covering the 2θ range of 10 to 60°. The determination of the pore size distribution and specific surface area was carried out using N_2 adsorption-desorption isotherms, which were measured with a Micromeritics ASAP 2020 porosimetry system at 77 K. Fourier transform infrared (FTIR) measurements were conducted using a Horiba FT-720 spectrophotometer, employing the KBr method, within the wavenumber range of 500–4000 cm^{-1}. The diffuse reflectance spectra (DRS) were recorded using a Hitachi U-4100 UV–visible-NIR spectrophotometer, covering the 200 – 800 nm range.

Photodegradation of micropollutants over 1DBCN

The photoactivity of the materials was investigated in the presence of visible light and PMS for the degradation of the target compound TC. The experiments were conducted in a photoreactor equipped with 400 W solar light lamps sourced from Taiwan with a UV cutoff (λ < 420 nm) (Omron, Taiwan). To initiate

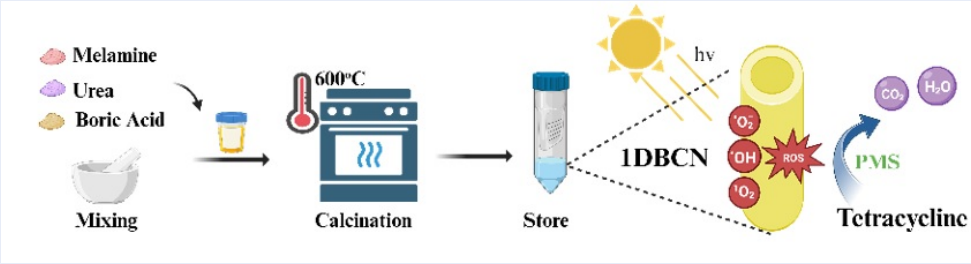

Scheme 1: Schematic illustration of 1D B-doped GCN (1DBCN) fabrication for sulfate activation toward tetracycline oxidation under visible light irradiation.

the degradation reaction, 50 mg of the catalyst was added to 100 mL of the solution under ultrasonication and then magnetically stirred in the dark for 30 minutes until adsorption-desorption equilibrium was achieved. Next, the photodegradation reaction was initiated by adding PMS to the system while maintaining magnetic stirring. At specific time intervals, a sample of the reaction solution was collected and filtered through a 0.22 μm pore membrane filter. The concentration of TC was determined using a UV–vis Hitachi UH5300, with a detection wavelength of 360 nm.

RESULTS

Characterization of the photocatalyst

The morphology of the 2D GCN is depicted in Figure 1a, whereas the tube-like material in Figure 1b has been shaped from the 1D tube-shaped material. The difference in morphology can be attributed to the variation in mass ratio between the melamine and urea. Because of the 1:1 mass ratio, the melamine and urea molecules are more randomly arranged in two-dimensional (2D) sheets, resulting in a thicker, irregular structure. However, a 1:10 mass ratio of melamine to urea leads to the formation of 1D nanotubes that are approximately 3 μm in length and 300 nm in diameter. It should be noted that the introduction of B into GCN maintains the hollow structure with open ends, as observed in the SEM image (Figure 1c,d). This unique shape and structure allow for an extensive surface area, providing an excellent platform for catalysis and chemical reactions.

Based on the provided weight percentages and atomic percentages, the B doping ratio in the sample is approximately 5.96% wt by atomic composition. This indicates that B was introduced into the material, contributing to its overall composition. The nitrogen adsorption-desorption method provides information on the porosity, pore size distribution, and material surface area. In Figure 3a, all samples exhibited type IV isotherms with a hysteresis loop at higher relative pressures (P/P_0=0.84-0.99), indicating the presence of mesopores and macropores. The specific surface area of 1DBCN (81.1 m^2/g) was approximately 1.4 and 2.3 times greater than that of 1DGCN (56.56 m^2/g) and 2DGCN (35.4 m^2/g), respectively. The pore diameter of the synthesized products ranged from 2 to 160 nm. The tubular structure of the nanomaterials provides more exposed surface area than does the 2D stacking layer, leading to enhanced reactivity and increased efficiency.

The crystal properties and chemical composition information were further analyzed using XRD and FT-IR spectroscopy. As illustrated in Figure 3b, all the samples exhibited two characteristic peaks corresponding to GCN, which were located at approximately 13.1° and 27.3°. Moreover, FT-IR spectroscopy was used to characterize the chemical structure and properties of GCN. According to Figure 3c, the characteristic FT-IR signals associated with tri-s-triazine units (810 cm^{-1}), aromatic CN heterocyclics (1200–1700 cm^{-1}), and N-H stretching uncondensed amino groups (3000–3500 cm^{-1}) were simultaneously identified[11].

UV–Vis diffuse reflection spectroscopy was used to investigate the optical properties of the 2DGCN, 1DGCN and 1DBCN samples. The comparison between 2DGCN and 1DGCN reveals that the photoabsorption edges of 1DGCN and 1DBCN are slightly redshifted, as shown in Figure 3d. Using the Kubelka–Munk method from DRS, the band gaps (Eg) of samples 1BDCN and 2DGCN can be 2.7 eV and 2.8 eV, respectively, which are smaller than the band gap of bulk 2DGCN (2.82 eV). The addition of boron to 1BDCN resulted in a slight reduction in the band gap, which can be attributed to the presence of midgap states.

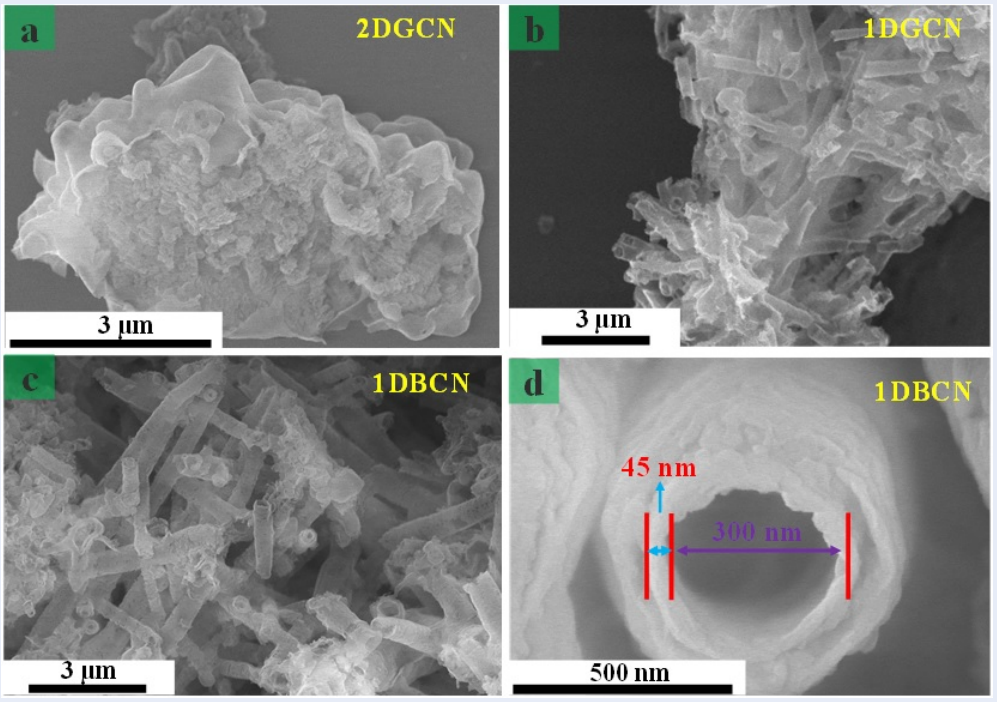

Figure 1: Morphology of (a) 2DGCN (2-dimensional sheet-like GCN was synthesized by 1 gram of melamine 1 gram of urea, forming an aggregate sheet-like structure approximately 5 μm in size), (b) 1DGCN (The tube morphology was synthesized using 1 gram of melamine and 10 grams of urea, which displayed a regular tubular structure), (c) The tube morphology was synthesized by 1 gram of melamine, 10 grams of urea, and 0.1 g of boric acid, maintaining a homogeneous tube structure (d) 1DBCN nanotubes (The material has a one-dimensional (1D) open hollow nanotube shape, with tube diameters ranging from 0.3 to 3 μm)

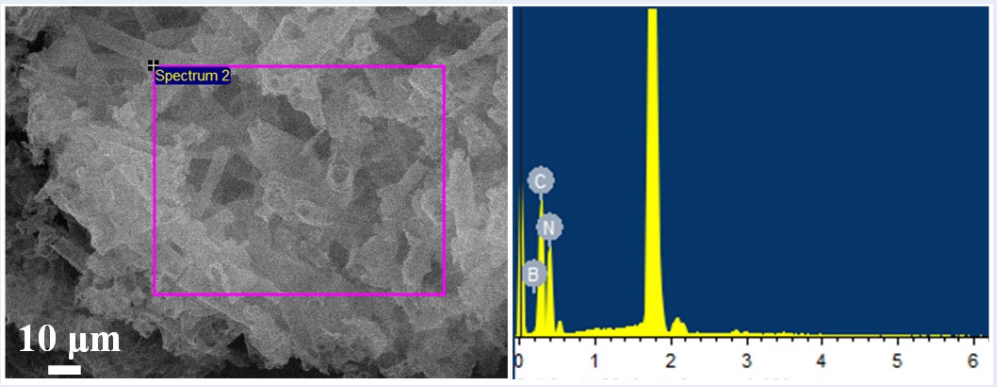

Figure 2: SEM-EDS analysis of boron-doped carbon nanotubes (1DBCN): Presence of a 5.96% boron atomic weight ratio doping within the hollow, one-dimensional structure

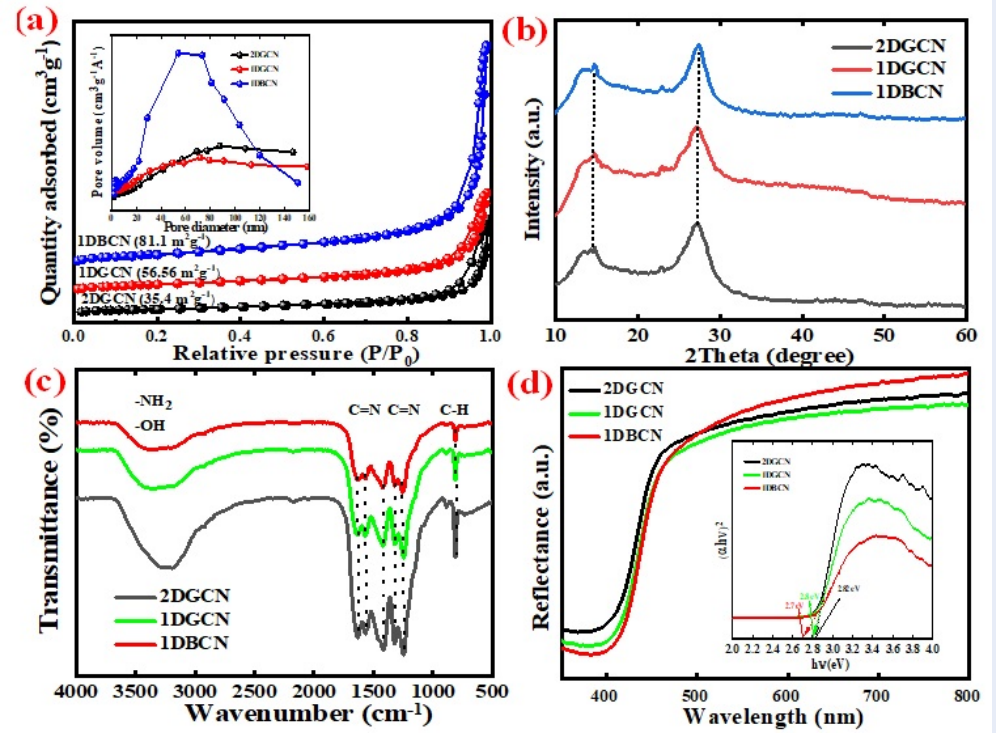

Figure 3: (a) The specific surface area of 1DBCN was 81.1 m^2/g, while 1DGCN had 56.56 m^2/g and 2DGCN had 35.4 m^2/g, the pore diameter of the produced products varied between 2 and 160 nm (b) XRD patterns of all the samples exhibited two characteristic peaks corresponding to graphitic carbon nitride (GCN), located at approximately 13.1° and 27.3°, (c) The chemical structures of all the materials were revealed to be similar by FT-IR spectroscopy, which is consistent with graphitic carbon nitride and (d) The UV–vis diffuse reflectance spectroscopy (UV–vis DRS) analysis showed the Eg of 1DBCN and 2DGCN.

Photodegradation performance

In some of the experiments, TC molecules were absorbed in the dark for 30 minutes to achieve adsorption equilibrium. Figure 4a illustrates the results obtained from the photolysis system in the absence of photocatalysts, where it can be observed that the TC concentration remained almost constant during the 30 minutes of light exposure. This observation indicates that in the absence of photocatalysts, the removal of TC was negligible.

When PMS and light were applied without the presence of a photocatalyst, the removal of TC was relatively low, with less than 20% of TC being eliminated. These results indicate that the effectiveness of visible light and PMS alone in removing TC is limited. However, upon the introduction of a photocatalyst in the presence of 0.3 mM PMS, a significant increase in the degradation of TC under visible light was observed. In particular, the transformation of 2D nanosheets into 1D nanotubes has proven to be advantageous for TC degradation. The 1DGCN nanotubes exhibited a significantly greater TC degradation efficiency, reaching 82%, than did the 2DGCN sample, which achieved 55% degradation. Remarkably, 1DBCN exhibited an enhanced TC removal efficiency of 99%, indicating that light irradiation-assisted PMS activation can efficiently promote TC oxidization.

To further evaluate the reaction kinetics, the rate constant (k) values were calculated using the pseudo-first-order kinetics model, as represented by Equation (1):

$$-\ln\left(\frac{C}{C_0}\right) = kt \quad (1)$$

In this equation, C_0 represents the initial TC concentration, C represents the TC concentration at a specific time, and k denotes the apparent first-order rate constant. For 1DBCN, the calculated rate constant (k) is 0.078 min^{-1}, indicating a photodegradation rate approximately 1.56 times faster than that of 1DGCN (k = 0.05 min^{-1}) and approximately 2.8 times faster than that of pristine 2DGCN (k = 0.027 min^{-1}). This comparison highlights the superior performance of 1DBCN in terms of its degradation rate of TC.

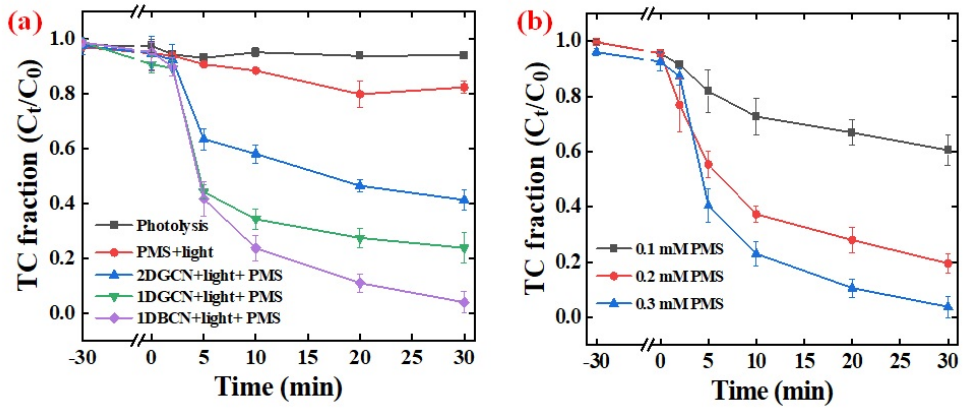

Figure 4: (a) Comparison of the TC degradation performances of 2DGCN, 1DGCN, and 1DBCN and (b) influence of the PMS concentration. The conditions (C_{TC} = 10 ppm, $C_{cat.}$ = 0.5 g/L, C_{PMS} = 0.3 mM, pH=7) (b) TC removal at different PMS concentrations over 1DBCN.

A further investigation was conducted to examine the impact of initial PMS concentration on TC degradation (Figure 4b). The results revealed that within a 30-minute timeframe, TC removal ratios of 17%, 80%, and 99% were achieved with PMS concentrations ranging from 0.1 mM to 0.3 mM. The 0.3 mM PMS concentration rate constant was determined to be 0.078 min^{-1}, which is greater than the rate constant for 0.2 mM PMS (0.026 min^{-1}) and significantly greater than the rate constant for 0.1 mM PMS (0.007 min^{-1}). As a result, the study revealed that increasing the PMS concentration significantly increased the photodegradation efficiency since higher concentrations of PMS generate reactive oxygen species (ROS), accelerating degradation. To gain a deeper understanding of the mechanism behind PMS activation assisted by boron-doped GCN nanotubes, radical quenching tests were performed. Tert-butanol (t-BuOH), p-benzoquinone (p-BQ), sodium azide (SA) and ammonium oxalate (AO) were used as scavengers to quench hydroxyl radicals ($^{\bullet}OH$), sulfate ($SO_4^{\bullet-}$) superoxide anions ($O_2^{\bullet-}$), singlet oxygen ($^1O_2$) and holes (h^+), respectively[12]. As shown in Figure 5a, AO, p-BQ, and SA significantly reduced TC degradation, while t-BuOH had a negligible effect. To gain further insight into the generation of these reactive species in the investigated systems, EPR spectroscopy was employed. The absence of peaks corresponding to these reactive species in the absence of light and PMS indicates that the activation of PMS solely by 1DBCN is insufficient to produce these reactive species. However, four triplet signal peaks corresponding to TEMP-$^1O_2$ (Figure 5b), four DMPO-$O_2^{\bullet-}$ signal peaks (Figure 5c), and seven signal peaks associated with the transformation of DMPO to DMPOX were detected (Figure 5d).

A series of catalytic experiments were conducted under identical reaction conditions to evaluate the recyclability of 1DBCN. Figure 6a shows that the degradation efficiency was consistently 82% throughout the experiment, even after five consecutive cycles. Additionally, a series of experiments, depicted in Figure 6b, were performed to assess the catalytic effectiveness of 1DBCN for different pharmaceutical compounds, including SMX and CIP. The results demonstrated that the degradation of all the compounds was successfully achieved within a 30-minute timeframe. In conclusion, these findings highlight the promising potential of the 1DBCN catalyst as a versatile agent for the oxidative degradation of diverse pharmaceutical compounds.

DISCUSSION

A tubular structure forms as a result of the high proportion of urea in the 1:10 mass ratio being converted into cyanuric acid, which forms a strong hydrogen bond with melamine molecules, resulting in supramolecular melamine-cyanuric acid structures[13]. Consequently, melamine and cyanuric acid are arranged in an orderly and regular manner, giving rise to a more uniform and symmetrical 1D tube-like shape upon calcination at 600°C. X-ray diffraction (XRD) analysis revealed two sharp peaks corresponding to the (100) and (002) planes, characteristic of the in-plane repeated tri-s-triazine units and interlayer stacking of conjugated aromatic systems, re-

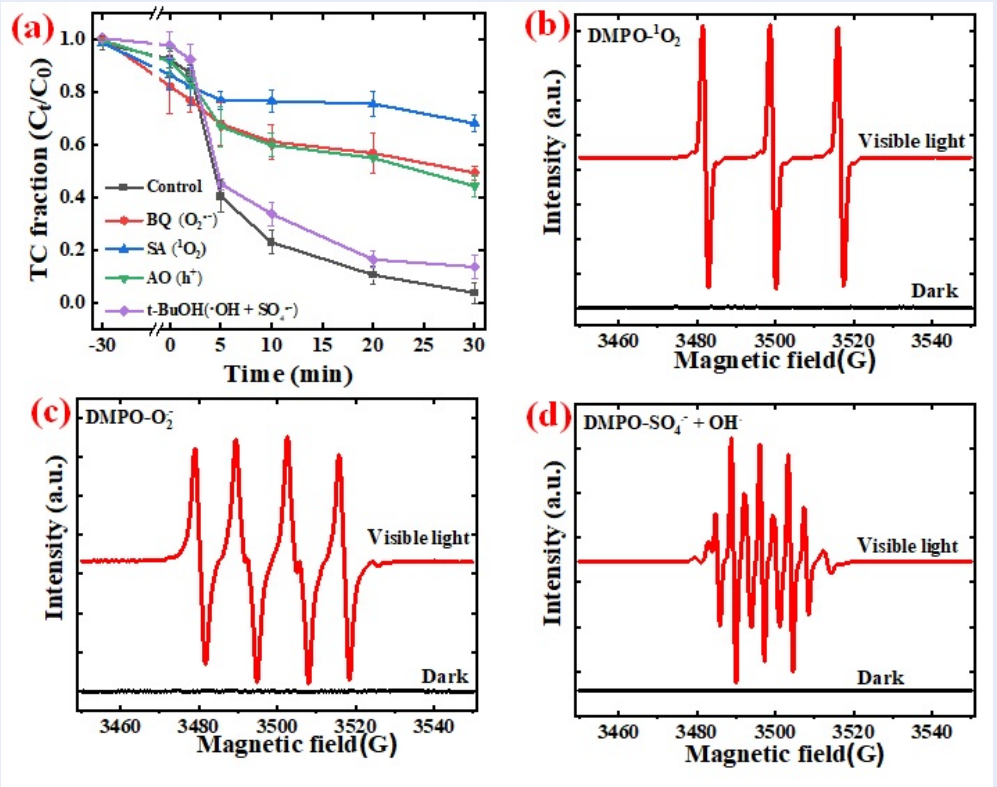

Figure 5: (a) Removal of TC with light-assisted PMS activation over 1DBCN in the presence of various scavengers. TC removal ratios after 30 min in the 1DBCN system with various scavengers. The conditions (C_{TC} = 10 ppm, $C_{cat.}$ = 0.5 g/L, C_{PMS} = 0.3 mM, pH=7), EPR patterns of (b) TEMPO -$^1O_2$, (c) DMPO $O_2^{\bullet-}$ and (d) DMPOX.

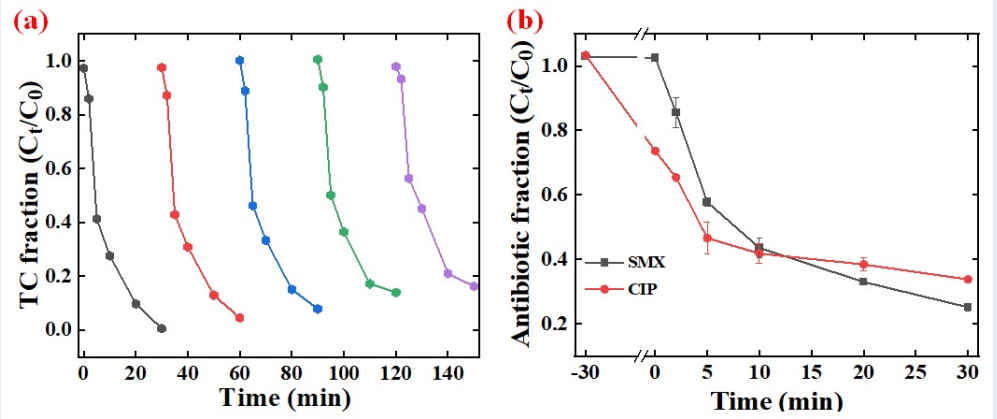

Figure 6: (a) Reusability of catalysts over five consecutive cycles of TC and (b) versatility of the 1DBCN catalyst with SMX and CIP.

spectively, in the GCN structure[14]. The peak corresponding to the (100) and (002) crystal planes in the 1DBCN sample does not exhibit any shift in angle or reduction in intensity. This indicates that the addition of boron (B) does not cause any significant changes to the lattice structure of GCN, likely due to the relatively low concentration of B present. Moreover, comparing the FT-IR spectra of the bulk GCN and the boron-doped GCN nanotubes showed no significant differences, suggesting that their chemical structures are identical[8]. This implies that the incorporation of boron dopants did not alter the fundamental chemical composition or bonding configuration of the GCN framework[11].

In addition to the structural aspects, surface area measurements provide further insights. The specific surface area of 1DBCN is approximately 1.4 times larger than that of 1DGCN and 2.3 times larger than that of 2DGCN. This is consistent with the fact that 1DGCN, with its distinct hollow structure, possesses a larger pore volume and specific surface area than 2DGCN. The presence of this rich hollow structure in 1DGCN contributes to its rich pore structure and high specific surface area. Furthermore, the specific surface area and average pore size of 1DBCN slightly increase, which can be attributed to the presence of boron. Boron facilitates the formation of a smoother surface and a tubular structure, consistent with previous research findings[15].

The incorporation of boron in 1DBCN has significant implications for its photocatalytic properties. The presence of boron-containing functional groups plays a crucial role in trapping exciton dissociation, thereby reducing electron-hole recombination. The boron-containing functional groups hinder exciton dissociation, reducing the recombination of electron-hole pairs. Moreover, the presence of boron facilitates the extraction of electrons from the π-conjugated structure due to the vacant 2pz orbital, which can significantly contribute to the improved photogenerated charge separation efficiency. Additionally, the B dopant can simultaneously reduce the bandgap to enhance light absorption, which is favorable for the activation of PMS and promotes electron transport, boosting the photocatalytic reaction[16].

To understand the mechanism behind the photocatalytic degradation process, radical quenching tests and electron paramagnetic resonance (EPR) spectroscopy were conducted. These experiments confirmed that h^+, $O_2^{\bullet-}$ and $^1O_2$ are the most reactive and are responsible for the majority, while $SO_4^{\bullet-}$ and $^{\bullet}OH$ contribute little to the photocatalytic degradation of TC over 1DBCN. The proposed reaction mechanism involves two steps: direct photoexcitation of 1DBCN to produce H^+ and $O_2^{\bullet-}$ and subsequent activation of PMS to generate $SO_4^{\bullet-}$ and $^{\bullet}OH$ and $^1O_2$. This synergistic system between the photocatalyst and PMS enables the efficient transfer of photogenerated electrons, facilitating the decomposition of organic molecules into smaller molecules.

According to these findings, possible reaction mechanisms in the PMS-photocatalysis synergistic system were proposed (Scheme 2). Upon exposure to light, photogenerated electrons (e^-) and h^+ were generated. The photoexcited e^- in the conduction band (CB) of 1DBCN reacts with O_2 to produce superoxide anions ($O_2^{\bullet-}$) ($O_2 \rightarrow O_2^{\bullet-}$, E_H = -0.33 eV vs. NHE)[17]. Simultaneously, with the addition of PMS to the system, e^- can reduce PMS, leading to the formation of sulfate radicals ($SO_4^{\bullet-}$), while holes (h^+) can react with HSO_5^- to form $SO_5^{\bullet-}$ (Equations (3) and (4)). The formation of singlet oxygen ($^1O_2$) can occur through multiple steps involving SO_5^- or $O_2^{\bullet-}$ in several steps (Equations (5), (6), and (7))[18]. Finally, h^+, $^{\bullet}OH$, SO_4^-, $O_2^{\bullet-}$, and $^1O_2$ contribute to the efficient degradation of TC.

Photocatalysts + $h\nu \rightarrow h^+ + e^-$ (1)

$e^- + O_2 \rightarrow O_2^{\bullet-}$ (2)

$HSO_5^- + e^- \rightarrow SO_4^{\bullet-} + OH^-$ (3)

$HSO_5^- + h^+ \rightarrow SO_5^{\bullet-} + OH^-$ (4)

$2SO_5^{\bullet-} \rightarrow 2SO_4^{\bullet-} + {}^1O_2$ (5)

$SO_4^{\bullet-} + OH^- \rightarrow SO_4^{2-} + {}^{\bullet}OH$ (6)

$^{\bullet}O_2^- + 2H_2O \rightarrow {}^1O_2 + H_2O_2 + 2H^+$ (7)

Consequently, the presence of $O_2^{\bullet-}$, $^{\bullet}OH$, h^+, $^1O_2$, and $SO_4^{\bullet-}$ can efficiently decompose TC in the photocatalytic process.

To assess and compare the effectiveness of our research findings with those of other studies, Table 1 has been compiled to present the efficiency of various photocatalysts in degrading specific pollutants under different experimental conditions.

Overall, Table 1 shows the effectiveness of various photocatalysts in degrading different pollutants. This highlights the superior performance of the synthesized 1DBCN photocatalyst in terms of pollutant degradation efficiency within the given time frame. Moreover, this evaluation offers valuable insights into the recyclability and versatility of the 1DBCN catalyst. This study emphasizes the effectiveness and durability of the catalyst, further highlighting its efficiency in the oxidative degradation of diverse pharmaceutical compounds. The remarkable catalytic activity exhibited by the 1DBCN catalyst positions it as a highly promising candidate for various applications in the field. These findings underscore the potential of the 1DBCN catalyst as a versatile and efficient tool for addressing environmental and pharmaceutical challenges.

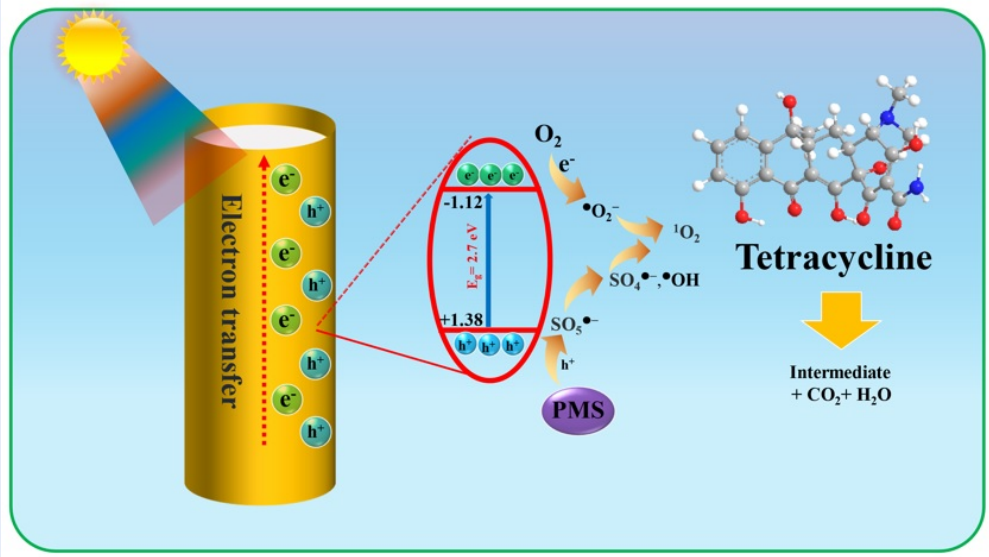

Scheme 2: The possible mechanism for TC photodegradation over 1DBCN for PMS activation under visible light irradiation

Table 1: Efficiency of different photocatalysts in degrading specific pollutants under varying conditions

Photocatalyst	[Catalyst] (g/L)	[PMS]	Pollutant conc. (mg/L)	Efficiency (%)	Time (min)	Light	Ref.
Se-g-C_3N_4	0.2	0.4 g/L	SMX =10	93.0	180	-	[19]
g-C_3N_4@NPC	0.08	0.1 g/L	RhB = 100	96.7	20	-	[20]
OCN/Py	0.16	0.5 mM	TC = 10	97.37	60	350 W	[14]
1DBCN	0.5	0.3 mM	TC = 10	99.0%	30	400 W	This study

CONCLUSIONS

In this study, B-doped GCN nanotubes were prepared by calcining a mixture of melamine, urea, and boric acid in an air atmosphere at high temperatures. The interaction between PMS and B-doped GCN nanotubes leads to the formation of reactive oxygen species, which efficiently catalyze the photocatalytic degradation of TC, resulting in a high removal efficiency. B-doped GCN nanotubes exhibited superior photocatalytic activity to that of pristine GCN nanotubes. In the presence of PMS and photocatalyst, the system generates abundant reactive species, including $O_2^{\bullet-}$, $^\bullet$OH, h^+, $^1O_2$, and $SO_4^{\bullet-}$, for improved photocatalytic activity. The removal efficiency of TC can reach 99%. Moreover, the concentration of PMS also affects the photodegradation rate, with the highest photodegradation rates observed in solutions with higher PMS concentrations. This study suggested that B-doped GCN nanotubes could be promising candidates for efficiently removing organic pollutants from wastewater.

ACKNOWLEDGMENTS

The authors would like to extend their appreciation to the Vietnam Ministry of Education and Training for the financial support provided under grant number B2023-TNA-23.

ABBREVIATIONS

PMS: Peroxymonosulfate
GCN: Graphitic carbon nitride
2DGCN: Graphitic carbon nitride nanosheet
1DGCN: Graphitic carbon nitride nanotubes
1DBCN: B-doped GCN nanotubes
ROS: Reactive oxygen species
TC: Tetracycline

DECLARATION OF GENERATIVE AI IN SCIENTIFIC WRITING

The readability and language of this work were enhanced by the use of the Chat GPT tool. The authors edited and reviewed after utilizing this tool.

AUTHOR CONTRIBUTIONS

Nguyen Thuy Giang: Conceptualization, Methodology, Software, Formal analysis, Writing – original draft, Visualization, Writing – review & editing. Nguyen Duy Hai: Validation, Resources, Writing – review & editing. Phan Dinh Quang: Software, Formal analysis, Editing. Vu Hoang Huong: Conceptualization, Methodology, Writing – review & editing. Nguyen Viet Hung: Conceptualization, Validation, Editing. Nguyen Manh Dung: Conceptualization, Methodology, Data curation, Writing – review & editing.

CONFLICT OF INTEREST

The authors declare that they have no competing interests.

REFERENCES

1. Wang C, et al. Investigation of antibiotic resistome in hospital wastewater during the COVID-19 pandemic: is the initial phase of the pandemic contributing to antimicrobial resistance? Environ Sci Technol. 2022;56(21):15007-18;Available from: http://10.1021/acs.est.2c01834.
2. Xu L, et al. Occurrence, fate, and risk assessment of typical tetracycline antibiotics in the aquatic environment: A review. Sci Total Environ. 2021;753:141975;Available from: http://10.1016/j.scitotenv.2020.141975.
3. Zhang H, et al. Novel sulfur vacancies featured MIL-88A (Fe)@CuS rods activated peroxymonosulfate for coumarin degradation: Different reactive oxygen species generation routes under acidic and alkaline pH. Process Saf Environ Prot. 2022;166:11-22;Available from: http://10.1016/j.psep.2022.07.060.
4. Zheng X, et al. Metal-based catalysts for persulfate and peroxymonosulfate activation in heterogeneous ways: A review. J Chem Eng. 2022;429:132323;Available from: http://0.1016/j.cej.2021.132323.
5. Shi H, et al. Efficient degradation of tetracycline in real water systems by metal-free g-C3N4 microsphere through visible-light catalysis and PMS activation synergy. Sep Purif Technol. 2022;280:119864;Available from: http://10.1016/j.seppur.2021.119864.
6. Balakrishnan A, et al. Removal of tetracycline from wastewater using g-C3N4 based photocatalysts: A review. Environ Res. 2022;114660;Available from: http://10.1016/j.envres.2022.114660.
7. Jiao Y, et al. Novel BN-Co surface bonding states constructed on hollow tubular boron doped g-C3N4/CoP for enhanced photocatalytic H2 evolution. J Colloid Interface Sci. 2021;595:69-77;Available from: http://10.1016/j.jcis.2021.03.134.
8. Lei L, et al. In situ growth of boron doped g-C3N4 on carbon fiber cloth as a recycled flexible film-photocatalyst. Ceram Int. 2021;47(1):1258-67;Available from: http://10.1016/j.ceramint.2020.08.246.
9. Yan S, Li Z, Zou Z. Photodegradation of rhodamine B and methyl orange over boron-doped g-C3N4 under visible light irradiation. Langmuir. 2010;26(6):3894-901;Available from: https://doi.org/10.1021/la904023j.
10. Liu Q, et al. Unraveling the roles of hot electrons and cocatalyst toward broad spectrum photocatalytic H2 generation of g-C3N4 nanotube. Solar RRL. 2021;5(6):2000504;Available from: http://10.1002/solr.202000504.
11. Huang H, et al. Synthesis and modification of ultrathin g-C3N4 for photocatalytic energy and environmental applications. Renew Sustain Energy Rev. 2023;173:113110;Available from: http://10.1016/j.rser.2022.113110.
12. Li Q, et al. Visible-light-driven N and Fe codoped carbon dots for peroxymonosulfate activation and highly efficient aminopyrine photodegradation. J Chem Eng. 2022;443:136473;Available from: http://10.1016/j.cej.2022.136473.
13. Nguyen MD, et al. Fabrication of visible-light-driven tubular F, P-codoped graphitic carbon nitride for enhanced photocatalytic degradation of tetracycline. J Environ Chem Eng. 2022;10(1):106905;Available from: http://10.1016/j.jece.2021.106905.
14. Fang H, et al. Oxygen-doped and pyridine-grafted g-C3N4 for visible-light driven peroxymonosulfate activation: Insights of enhanced tetracycline degradation mechanism. Sep Purif Technol. 2023;314:123565;Available from: http://10.1016/j.seppur.2023.123565.
15. Kharatzadeh E, Khademalrasool M. Synthesis of S-doped g-C3N4 nanostructures by reflux method and study of photocatalytic and photoelectrochemical performances. Ceram Int. 2024;Available from: http://10.1016/j.ceramint.2024.02.144.
16. Wu L, et al. Coordination-driven boron and copper on carbon nitride for peroxymonosulfate activation to efficiently degrade organic contaminants. Sep Purif Technol. 2023;312:123349;Available from: http://10.1016/j.seppur.2023.123349.
17. Bai X, et al. Fe-g-C3N4/reduced graphene oxide lightless application for efficient peroxymonosulfate activation and pollutant mineralization: Comprehensive exploration of reactive sites. Sci Total Environ. 2023;855:158799;Available from: http://10.1016/j.scitotenv.2022.158799.
18. Jing L, et al. Advanced oxidation via the synergy of C-defective/C-O band modified ultrathin porous g-C3N4 and PMS for efficient photothermal degradation of bisphenol pollutants and lignin derivatives. Green Energy Environ. 2023;Available from: http://10.1016/j.gee.2023.01.006.
19. Tian Y, et al. Enhanced peroxymonosulfate decomposition into OH and 1O2 for sulfamethoxazole degradation over Se doped g-C3N4 due to induced exfoliation and N vacancies formation. Sep Purif Technol. 2021;267:118664;Available from: http://10.1016/j.seppur.2021.118664.
20. Kong LH, et al. Combination of N-doped porous carbon and g-C3N4 for effective removal of organic pollutants via activated peroxymonosulfate. J Environ Chem Eng. 2022;10(3):107808;Available from: https://doi.org/10.1016/j.jece.2022.107808.